

See discussions, stats, and author profiles for this publication at: <https://www.researchgate.net/publication/271831600>

Resonance Raman and Excitation Energy Dependent Charge Transfer Mechanism in Halide Substituted Hybrid Perovskite Solar Cells

ARTICLE in ACS NANO · FEBRUARY 2015

Impact Factor: 12.88 · DOI: 10.1021/nn507345e

CITATIONS

8

READS

189

6 AUTHORS, INCLUDING:



[Byung-wook Park](#)

Ulsan National Institute of Science and Tech...

25 PUBLICATIONS 257 CITATIONS

[SEE PROFILE](#)



[Sagar Motilal Jain](#)

Uppsala University

10 PUBLICATIONS 37 CITATIONS

[SEE PROFILE](#)



[Anders Hagfeldt](#)

École Polytechnique Fédérale de Lausanne

391 PUBLICATIONS 31,907 CITATIONS

[SEE PROFILE](#)



[Gerrit Boschloo](#)

Uppsala University

197 PUBLICATIONS 14,077 CITATIONS

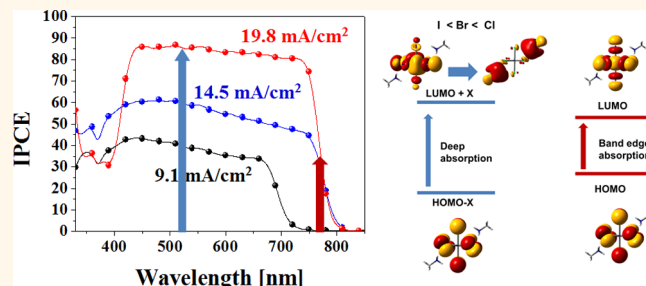
[SEE PROFILE](#)

Resonance Raman and Excitation Energy Dependent Charge Transfer Mechanism in Halide-Substituted Hybrid Perovskite Solar Cells

Byung-wook Park,[†] Sagar M. Jain,[†] Xiaoliang Zhang,[†] Anders Hagfeldt,^{†,§} Gerrit Boschloo,^{*,†} and Tomas Edvinsson^{*,‡}

[†]Department of Chemistry-Ångström Laboratory, Physical Chemistry, Uppsala University, Box 523, SE 751 20 Uppsala, Sweden, [‡]Department of Chemistry-Ångström Laboratory, Inorganic Chemistry, Uppsala University, Box 538, SE 751 21 Uppsala, Sweden, and [§]Laboratory for Photomolecular Science (LSPM), Swiss Federal Institute of Technology at Lausanne (EPFL), CH-1015, Lausanne, Switzerland

ABSTRACT Organo-metal halide perovskites (OMHPs) are materials with attractive properties for optoelectronics. They made a recent introduction in the photovoltaics world by methylammonium (MA) lead triiodide and show remarkably improved charge separation capabilities when chloride and bromide are added. Here we show how halide substitution in OMHPs with the nominal composition $\text{CH}_3\text{NH}_3\text{PbI}_2\text{X}$, where X is I, Br, or Cl, influences the morphology, charge quantum yield, and local interaction with the organic MA cation. X-ray diffraction and photoluminescence data demonstrate that halide substitution affects the local structure in the OMHPs with separate MAPbI_3 and MAPbCl_3 phases. Raman spectroscopies as well as theoretical vibration calculations reveal that this at the same time delocalizes the charge to the MA cation, which can liberate the vibrational movement of the MA cation, leading to a more adaptive organic phase. The resonance Raman effect together with quantum chemical calculations is utilized to analyze the change in charge transfer mechanism upon electronic excitation and gives important clues for the mechanism of the much improved photovoltage and photocurrent also seen in the solar cell performance for the materials when chloride compounds are included in the preparation.



KEYWORDS: mixed halide perovskites · solution processing · solar cells · Raman spectroscopy · charge separation mechanism · density functional theory

Organic–metal halide perovskites (OMHPs) were first synthesized in 1978^{1,2} but have received much scientific attention after their recent introduction as a photovoltaic material with very low cost and intriguing properties. The first report of use of OMHPs in a solar cell was made by Miyasaka *et al.* in 2009,³ who used methylammonium lead triiodide (MAPbI_3) and methylammonium lead tribromide (MAPbBr_3) as absorber material deposited on mesoporous TiO_2 in photoelectrochemical solar cells. Significant improvements in device performance and stability were found when the same materials were introduced in a solid-state dye-sensitized solar cell device structure, *i.e.*, in a structure where the liquid electrolyte was replaced

by a molecular hole conductor, and efficiencies close to 10% were reported in initial studies.^{4,5} The power conversion efficiency (PCE) has significantly improved with the increased research efforts of recent years,^{6–9} where Sang-il Seok and co-workers (Korea Research Institute of Chemical Technology, KRICT) hold the present record with 20.1% (certified).¹⁰ It has become apparent that the organic–inorganic metal halide perovskites, and specifically MAPbI_3 with addition of chloride, have many intriguing properties that need detailed investigation for a full understanding. One of the aspects that has raised a lot of speculation is the possible function of the much improved photocurrent and photovoltage when adding chloride to the system and in particular its

* Address correspondence to gerrit.boschloo@kemi.uu.se, tomas.edvinsson@kemi.uu.se.

Received for review December 23, 2014 and accepted February 4, 2015.

Published online
10.1021/nn507345e

© XXXX American Chemical Society

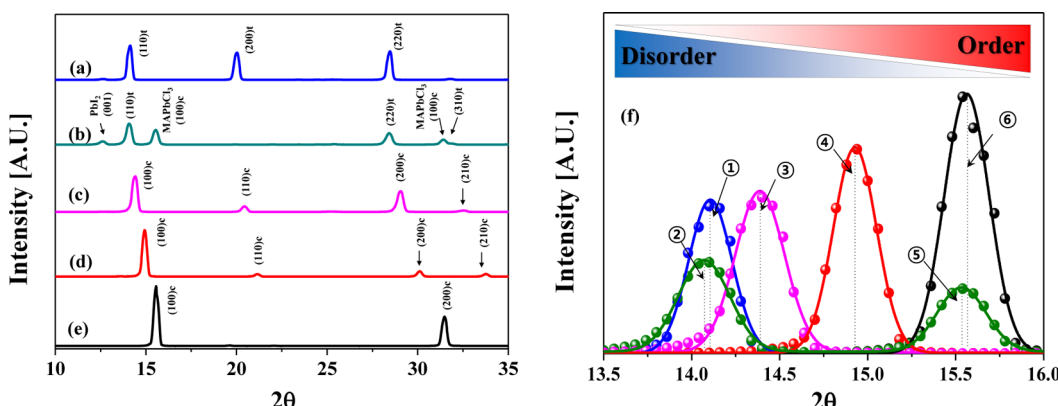


Figure 1. Full XRD spectra summarized for OMHPs, *viz.*, (a) MAPbI₃, (b) MAPbI₂Br, (c) MAPbI₂Cl, (d) MAPbBr₃, and (e) MAPbCl₃. (f) Extracted XRD patterns of preferred orientation in the range 13.0–16.5 2θ from XRD patterns of the left panel: ① MAPbI₃, ② MAPbI₃ in MAPbI₂Cl, ③ MAPbI₂Br, ④ MAPbCl₃ in MAPbI₂Cl, ⑤ MAPbBr₃, ⑥ MAPbCl₃.

effect on the interplay with the organic MA cation in the OMHP structure. Not only is it a rather bulky cation, it also has a dipole moment and protons that may be involved in hydrogen bonding. Furthermore, if the dipolar MA ion is liberated so it can rotate, it can contribute to a ferroelectric effect as well as a dynamic alignment and thus a more effective charge screening and separation. Here we address these issues with an investigation of the effects of the organic cation when using different halides in the OMHPs.

In other studies, partial substitution of the iodide in MAPbI₃-based solar cells by introducing bromide (Br) and chloride (Cl) was found to improve the performance and stability of the devices.^{11–13} Inclusion of bromide changes the crystalline phase of the OMHP from tetragonal to cubic for Br:I ratios larger than 1:4.^{11,14} Small amounts of Cl in MAPbI₃ appear to increase the charge mobility.^{12,13} It is, however, still largely unclear why Cl and Br inclusion leads to improved solar cell performance. Mosconi *et al.* performed computational calculations for the different trihalide modifications to MAPbX₃ (X = Cl, Br, I) and MAPb₂X, to investigate the role played by these halides in OMHPs with respect to the electronic, optical, and structural properties.¹⁵ They suggested that hydrogen bonding between the ammonium groups and the halides in OMHPs is an important factor for the properties and stability of the materials.

We investigate the role of the halide by performing correlating investigations between chemical and physical properties for halide substitution in OMHPs during the preparation processes. Raman spectra for different crystalline phases of prototypical MAPbI₃ have recently been reported,¹⁶ but the mechanistic function of the halides in the properties of the organic cation within an inorganic octahedron framework has so far been unclear. The crystalline growth through a disordered to ordered phase transition has previously been investigated in MAPbI₃ at different temperatures.¹⁷ Here, we investigate the relationship between the inorganic

cage and an organic molecule for three substances during the synthesis process, namely, MAPbI₃, MAPbI₂Br, and MAPbI₂Cl prepared with the respective methylamine halides (MAX), by cross-correlating X-ray diffraction (XRD), photoluminescence (PL), UV-visible spectroscopy, Raman spectroscopy, and density functional theory (DFT) calculations. In particular, the different halide-substituted OMHPs are investigated (see Figure 1) in order to understand the relationship between the local structure of OMHPs and the dynamics of the organic MA cation and the halides. These effects seem to be significantly related to charge separation and transport efficiency for thin-film solar cell systems of OMHPs.

RESULTS

OMHP layers with the nominal compositions MAPbX₃ and MAPb₂X, where X is I, Cl, or Br, were deposited onto microscope glass by spin coating the precursor solution, followed by heating to 100 °C; see Methods section for details. XRD patterns of the resulting films are shown in Figure 1a and b. The MAPbI₃ film shows a tetragonal crystalline perovskite phase in good agreement with literature,^{8,17} while MAPbBr₃ and MAPbCl₃ show a cubic structure. The XRD peak positions, calculated lattice distances (*d*-spaces), and crystal sizes from full width at half-maximum (fwhm) are summarized in Table S1. It is known that MAPb(I_{1-x}Br_x)₃ exists in a tetragonal phase for x < 20% of total halide and in the cubic phase for x > 20%.¹¹ In this study, MAPbI₂Br (equimolar ratio between PbI₂ and MABr) was indeed found to be cubic, consistent with previous observations. MAPbI₂Br shows a single-phase XRD pattern with a main peak assigned to (100)c, shifted 0.28° toward a higher angle compared to (110)t of MAPbI₃. The OMHP with nominal composition MAPbI₂Cl (equimolar ratio between PbI₂ and MACl) contained subcrystals of MAPbI₃ and MAPbCl₃, but does not contain a halide mixed phase, which is in good agreement with previous investigations.^{12,13,17}

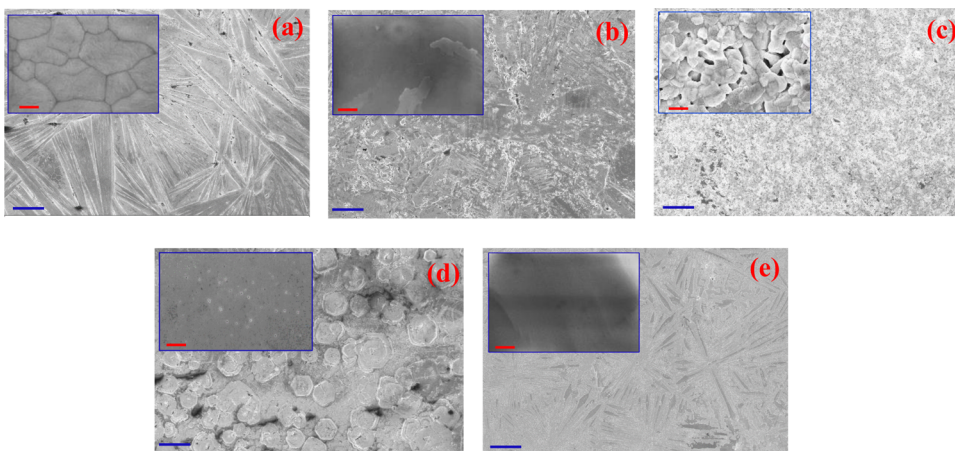


Figure 2. Surface morphologies for (a) MAPbI_3 , (b) MAPbI_2Br , (c) MAPbI_2Cl , (d) MAPbBr_3 , and (e) MAPbCl_3 (the scale of black color: $40 \mu\text{m}$) with inset figures magnifying each surface morphology (scale of red color: 200 nm).

In comparison, the integrated XRD intensities of the MAPbI_3 and MAPbCl_3 peaks in Figure 1f can demonstrate a crystal ratio of 1.5:1 for these two materials, in good agreement with the relation of the compounds in the preparation procedure. Some traces of crystalline PbI_2 with a (001) orientation were also found, similar to previous investigations.⁸ It has been reported that residual PbI_2 may give rise to a passivation effect in OMHP solar cells.¹⁸ In previous investigations,^{17,19} the crystallinity of MAPbI_3 films, prepared under the same conditions as here, was only 30% at best, while the remainder was amorphous material. A slow crystallization process of self-assembly was found to proceed during weeks of aging such as second-order phase transition, which is related to thermodynamic entropy effects with crystalline growth.¹⁷ In this investigation, we observe a first-order phase transition^{20,21} owing to chemically substituted halides with a decreasing lattice spacing and increasing intensities in the order MAPbI_3 , MAPbI_2Br , MAPbBr_3 , and MAPbCl_3 , as summarized in Table s1 and Figure 1f. In particular, subcrystallites of MAPbI_3 and MAPbCl_3 , during the mixed I/Cl halide preparation, are obtained with values of lattice spacing in good agreement with those of pure MAPbI_3 and MAPbCl_3 but with approximately 17% reduction in grain sizes. The lattice spacing is slightly shifted to lower angle with diminishing intensities, consistent with a disorder phase transition, agreeing with previously reported results.¹⁷ The SEM images depicted in Figure 2a–e show that the halide modification in MAPbX_3 has a significant effect on the resulting surface morphologies of the perovskites. Although the crystal sizes estimated from XRD are quite similar (23–28 nm, see Table s1), the surface morphologies differ much in the submicrometer scale. MAPbI_3 displays smooth sections with irregular boundaries with a collective crystallite size of 200 to 600 nm. MAPbI_2Cl films contain 180–190 nm sized crystals with mixed subcrystals of MAPbI_3 and MAPbCl_3 according to the XRD result. The MAPbI_2Br and MAPbCl_3 films appear very smooth in high magnification, whereas

the MAPbBr_3 film shows hexagonal micrometer crystallites. The submicrometer scale, however, indicates very similar surface morphology to those of MAPbI_2Br and MAPbCl_3 . The SEM cross sections of mixed halide OMHPs, shown in Figure 5a, confirm this.

The optical properties of MAPbI_3 , MAPbI_2Br , and MAPbI_2Cl films are shown in Figure 3. In the absorption spectra of MAPbI_3 and MAPbI_2Cl an absorption onset at about 780 nm is found, corresponding to an optical band gap of about 1.6 eV, while that of MAPbI_2Br appears at 690 nm, which corresponds to an optical band gap of about 1.8 eV, in good agreement with the trend reported by Noh *et al.*¹¹ In comparison to the MAPbI_3 film, in the MAPbI_2Cl film (containing a two-phase mixture of MAPbI_3 and MAPbCl_3) an increasing absorption can be seen at wavelengths below 470 nm and further below 410 nm, which can be attributed to absorption in the PbI_2 and MAPbCl_3 fractions in this material, respectively.^{6,17}

Photoluminescence spectra for the same samples are shown in Figure 3b. MAPbI_3 has its peak emission at 775 nm (1.59 eV), while MAPbI_2Br has a blue-shifted peak at 700 nm (1.77 eV), in agreement with the band gap values of these semiconductors. MAPbI_2Cl has a significantly broadened emission spectrum, with a width at half-maximum approximately twice that of MAPbI_3 . A clear shoulder at 734 nm is found. The relative intensities of the photoluminescence were 1:2.5:6.5 for $\text{MAPbI}_3:\text{MAPbI}_2\text{Br}:\text{MAPbI}_2\text{Cl}$, respectively. Apparently, Br substitution as well as the use of the Cl precursor leads to OMHP materials where less of the created excitons are lost due to nonradiative decay processes, like that of a direct band gap semiconductor.²² Br substitution and a Cl precursor have an effect on the order of the inorganic sublattice but may also have an effect on the organic cation and the localization of excited-state charges, as investigated in more detail below.

The mechanism of changes in quantum efficiency has previously been investigated in inorganic

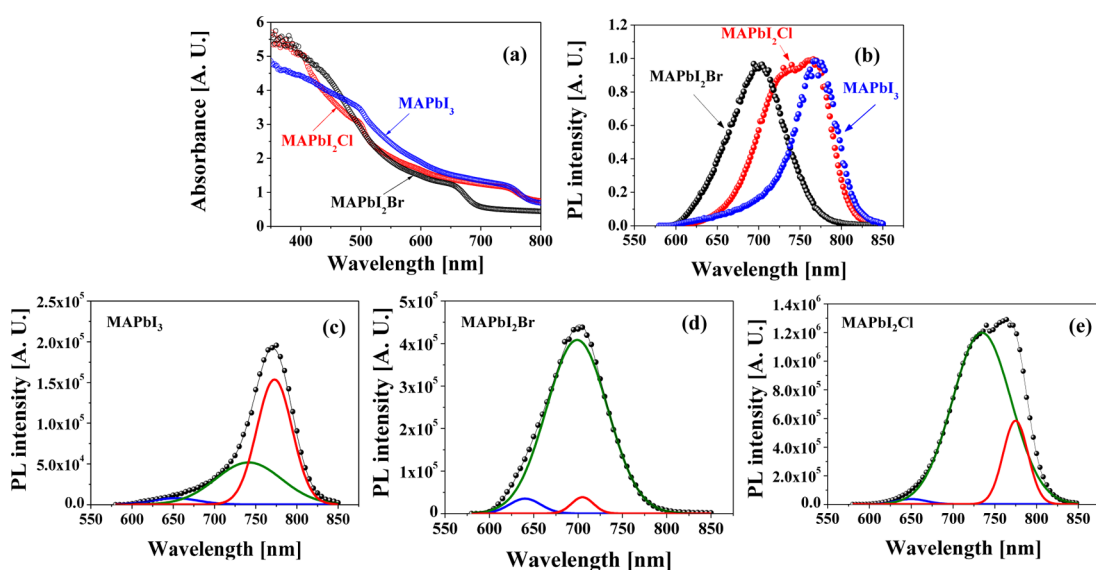


Figure 3. Optical properties of MAPbI₃, MAPbI₂Br, and MAPbI₂Cl thin films on glass. (a) Electronic absorption spectra. **(b)** Normalized steady-state photoluminescence spectra (pump fluence wavelength at 610 nm). **(c–e)** Deconvoluted spectra.

light-harvesting materials by peak fitting PL spectra.²³ In the same way, the crystalline constitutions of OMHPs can be analyzed by fitting PL spectra with Gaussian functions using three components, as shown in Figure 3c–e. Corresponding phase transitions of crystalline parts have previously been investigated on other inorganic light-harvesting and metal oxide materials.^{24,25} The blue curves of PL spectra in Figure 3c–e would then correspond to the optical band edge of orthorhombic-phased OMHPs assigned from the magnitude of the Stokes shift.²⁶ The two PL spectra of MAPbI₃ and MAPbI₂Cl indicate two constitutions, represented by the red and green curves in Figure 3c and e, where the two kinds of local phases may be distinguished as ordered and disordered crystallites. The curves demonstrate different fwhm, one with a width of 70–80 nm (disorder) and one with less than 30 nm (order). Since the total emission is proportional to the area under the PL curve, a comparison between the integrated areas can give an estimation of the relative difference of the quenching yield of the photogenerated charge carriers. MAPbI₃ shows a ratio of charge quenching yield (integral PL spectra)²⁷ of 1:1.6 for disordered and ordered phases, respectively. We can note that the PL spectrum of MAPbI₂Cl is not interfering with the fluorescence of MAPbCl₃ due to the huge difference in the PL intensity between MAPbI₂Cl and MAPbCl₃ as seen in Figure s4. The ratio of the charge carriers effective for the PL emission is 5:1 with respect to disordered and ordered phases of MAPbI₃ within the MAPbI₂Cl film. The energy shift of PL spectra for disordered and ordered phases in PbWO₄ monospecies has been addressed in the same way as in a previous study.²⁸ Following the same reasoning and comparing the PL behavior of the MAPbI₃ and MAPbI₂Cl materials, the effect of Cl-induced OMHP film

formation can consequently result in a significantly higher effective charge lifetime. For the Br substitution, on the other hand, the PL spectrum of the green curve on MAPbI₂Br indicates approximately 90% charge quenching yield, which can correspond to a disorder-phased crystallite, and the PL spectrum of the red curve can be assigned to an order-phased crystallite in Figure 3d.

The improved charge lifetime effect can thus be analyzed *via* the PL spectra and correlates with the order to disorder XRD patterns on bulk OMHPs. Nevertheless, the origin of the improved material properties by the halide-induced OMHPs is still not clear. We have performed Raman spectroscopy on the given OMHP clusters to obtain information on local phase transitions and charge separation/transfer mechanisms. There have been some previous Raman spectroscopy studies on OMHPs, but peak assignment is ambiguous in these studies and also they do not include possibilities to study vibrations below 60 cm⁻¹.¹⁶ Theoretically calculating the exact Raman shift from quantum mechanics is notoriously problematic due to the low energies that are evaluated. Theoretical results within 5–10 cm⁻¹ from the experimental values are more a matter of coincidence, and the order of the vibration peaks can be problematic if there is no clear experimental spectrum to compare with. Here, we have performed low-frequency Raman measurements (down to 10 cm⁻¹) and nonperiodic DFT calculations with emphasis on the ordering of the peaks to determine Raman properties of OMHPs. In particular, we investigate the fundamental vibrations in the isolated clusters and can follow the trends in the splitting of the degenerate states when different halogens are included in the structure. This can then form a strong basis for comparison with our experimental data as well as with previously performed periodic calculations.¹⁶

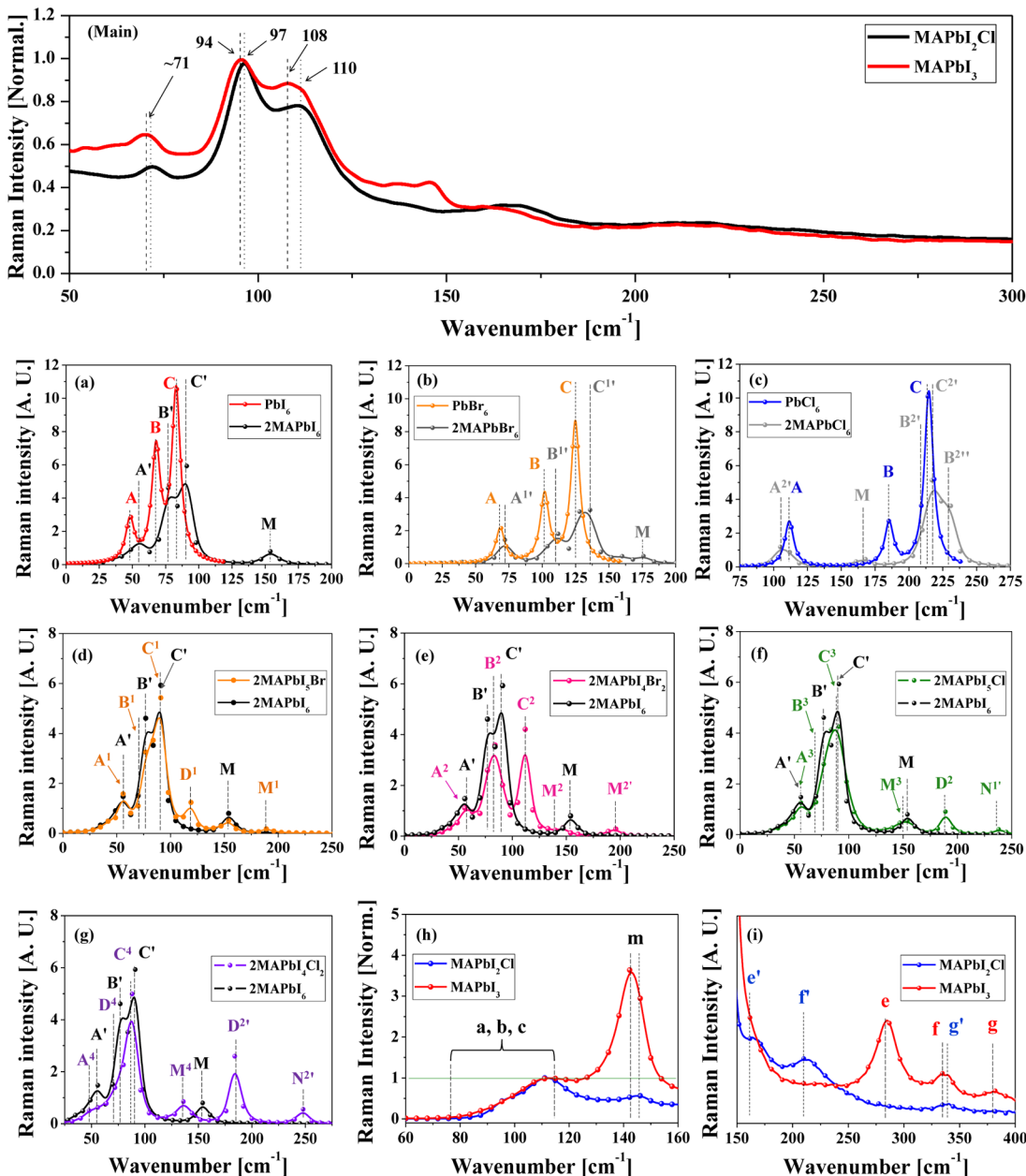
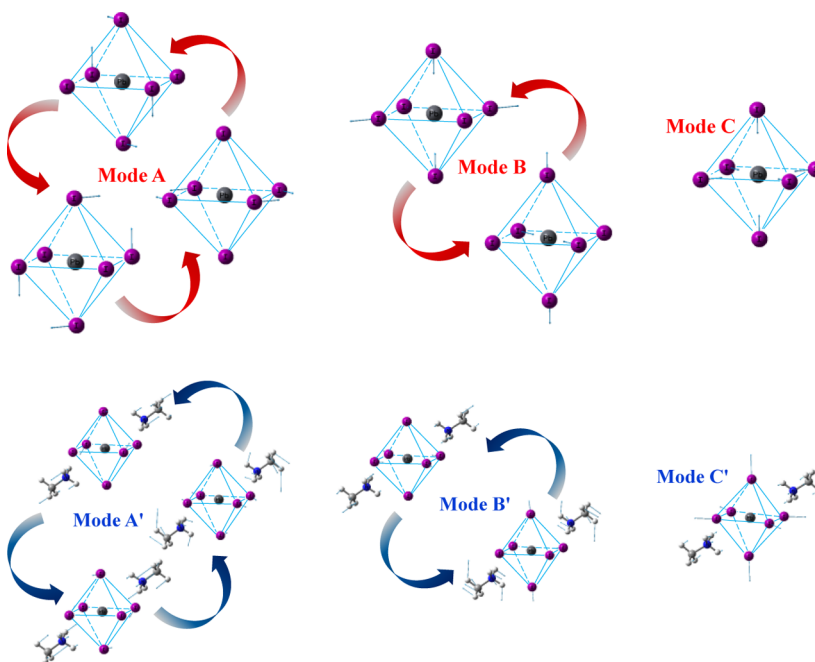


Figure 4. Experimental Raman spectra (main), DFT-calculated Raman spectra for (a) PbI_6 with 2 MAPbI_6 , (b) PbBr_6 with 2 MAPbBr_6 , and (c) PbCl_6 with 2 MAPbCl_6 , and comparison of 2 MAPbI_5Br , (d) 2 $\text{MAPbI}_4\text{Br}_2$, (e) 2 MAPbI_5Cl , and (f) 2 $\text{MAPbI}_4\text{Cl}_2$. (h, i) Normalized experimental Raman spectra recorded at very low laser intensity (<0.01 mW).

The experimental Raman spectrum for MAPbI_3 shows vibration peaks at 40, (54), (63), 71, 94, 108, 135, and 145 cm^{-1} , whereas MAPbI_2Cl shows corresponding peaks at 40, NA, NA, 71, 97, 110, and a broad peak at 166 cm^{-1} as seen in Figure 4 (see Supporting Information for resolved peaks under 60 cm^{-1}). With the NA (not applicable) notation, we want to emphasize that the peaks cannot be resolved and the spectra instead show a shoulder in that area. The 63 and 94 cm^{-1} vibration peak is in good agreement with the 62 and 94 cm^{-1} peak reported previously¹⁶ for MAPbI_3 , whereas our 63 cm^{-1} peak is very weak, and our assignment instead shows that our stronger 71 cm^{-1} peak is more likely to correspond to the

significant mode in this area. Experimental spectra in the previous study, however, showed that other peaks below 63 cm^{-1} were not resolved, making peak assignment problematic. Here we find peaks also at 40 and 54 cm^{-1} , whereas the strongest Raman peaks are found at 69–73, 94–97, and 108–110 cm^{-1} , with a small shift depending on halide composition during synthesis. To assist with the assignment, we perform theoretical vibration spectroscopy with DFT. In periodic DFT calculations, assumptions about the crystal symmetry of the system have to be made. This then provides a good model system for single-crystalline materials where the different orientation of the cations must be considered to be periodic. For the study of



Scheme 1. Three vibrational modes of inorganic octahedra (top figure) and bi-methylammonium-installed octahedra (bottom figure).

local effects in the inorganic octahedron and a non-periodic or noncrystalline behavior of the organic cation, cluster calculations on the other hand can be very informative. In the present approach, an inorganic octahedron unit cluster PbX_6 is used, and this cluster is combined with two MA-dipole canceling cations. A PbI_6 octahedron has 15 internal degrees of freedom ($3N - 3$, where N is the number of iodine atoms). In a group theoretical representation,²⁹ they can be written as $A_{1g} + E_g + 2T_{1u} + T_{2g} + T_{2u}$, where A_{1g} , E_g , and T_{2g} are Raman active, the two T_{1u} modes are IR active, and T_{2u} is a silent mode (neither Raman or IR active). Considering PbI_6 as a molecular unit within the lattice, it belongs to the O_h symmetry group, and any deviation from this symmetry would result in splitting of the degenerate states and eventually complete removal of symmetry and 15 different bands. For Raman one would thus expect three bands for the fully O_h symmetric PbI_6 and a splitting that would depend on the positions of the surrounding organic cations. Calculated Raman spectra for PbX_6 and $(\text{MA})_2\text{PbX}_6$ clusters are shown in Figure 4a–g, and experimental data for MAPbI_3 and MAPbI_2Cl are shown in Figure 4h and i. Notably, Raman spectra of Br-containing OMHPs could not be obtained in the experiment, because of strong fluorescence hiding the vibration information using either a 532, 633, or 785 nm laser. The calculated Raman signals for the octahedron clusters are summarized in Table S2, showing three different vibrational modes in Scheme 1: triply degenerate asymmetric X-Y, X-Z, and Y-Z vibrations (mode A), a double-degenerate asymmetric "breathing" (mode B), and symmetric "breathing" (mode C). Furthermore, the MA vibrations

(rotation, wagging, MA-MA stretch) are shown. In agreement with the group theoretical analysis, we observe three bands for the unperturbed PbX_6 clusters and a splitting of the degenerate states in the $(\text{MA})_2\text{PbX}_6$ clusters into six Raman-active vibrations. The Raman peaks in $(\text{MA})_2\text{PbX}_6$ clusters are generally shifted to higher wavenumbers (energy) compared to those in the PbX_6 clusters, which is caused by the organic cations that extend the motion of X from the Pb^{2+} atom. Assuming an ideal iodine-sharing network vibrating fully in phase, the higher wavenumbers in the symmetric clusters would then approach the phonon vibration limit. The calculated Raman spectrum of $(\text{MA})_2\text{PbCl}_6$ (see Figure 4c) differs somewhat from the other clusters. Mode A shifts to lower wavenumbers, and mode B appears as two peaks. Finally, all $(\text{MA})_2\text{PbX}_6$ structures show Raman activity of the MA groups between 140 and 180 cm^{-1} .

We also performed DFT calculations on mixed halide clusters, such as $(\text{MA})_2\text{PbI}_5\text{Cl}$ and $(\text{MA})_2\text{PbI}_4\text{Cl}_2$. A single Cl substitution does not result in large differences in calculated Raman vibrational spectra compared to the $(\text{MA})_2\text{PbI}_6$ cluster, while larger changes are found for two introduced Cl atoms. This can be used for assignments and vibrational signatures (D) that can identify doped phases. Figure 4f and g show Raman activities compared to the $(\text{MA})_2\text{PbI}_6$ cluster, which is assigned to asymmetric vibrations of Pb-I between 40 and 95 cm^{-1} . Moreover, there are two small appearances of additional vibration modes, for instance $\text{N}^{1'}$ (green color, N-Cl stretch via H at 240 cm^{-1}) and D^2 (green color, Pb-Cl stretch at 190 cm^{-1}) in Figure 4f. The case of $(\text{MA})_2\text{PbI}_4\text{Cl}_2$ with double Cl substitution in the

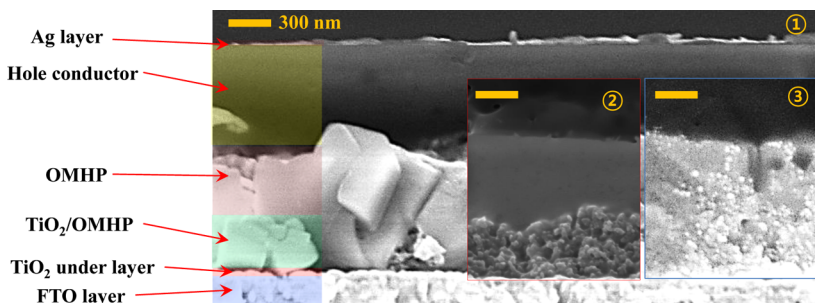


Figure 5. Cross sectional SEM images for thin-film solar cell devices ① MAPbI₂Cl, ② MAPbI₂Br, and ③ MAPbI₃ light-harvesting layers).

octahedral unit in Figure 4g has rather different vibration modes, *viz.*, mode D⁴ (violet color, asymmetric Pb–Cl stretch, 75–82 cm⁻¹) and highly increased intensity of mode D^{2/1} (violet color, asymmetric Pb–Cl stretch at 185 cm⁻¹) compared with mode D² (green colored solid line in Figure 4f). Moreover, in Figure 4g the Raman activity of mode M⁴ (violet color, at 138–143 cm⁻¹) is shown to shift to lower wavenumber compared to mode M³ (green color, Figure 4f), but mode N^{2/1} (violet color, at 247 cm⁻¹) is shifted to higher wavenumber for mode M^{2/1} (green color, Figure 4f). The inclusion of new vibration signatures and the relative intensity shifts in the Raman activities of (MA)₂PbI₄Cl₂ compared to the undoped analogue can thus be used to identify if there is local halide substitution or if the different halides are in two different phases. Both the single- and double-Cl-substituted OMHPs have the common signature of a decreased Raman intensity of modes C³ and C⁴ (green and violet colors) compared to mode C' (black color).

We first compare the DFT-simulated Raman spectra for three vibrational modes and the experimental Raman signal of MAPbI₃; see Figure 4a, h, and i. In MAPbI₃ three shoulders or peaks in the 70–120 cm⁻¹ range are found that are indicated with a, b, and c, which can be assigned to modes A, B, and C. Moreover, a further four peaks (m, d, e, and f) appear between 140 and 400 cm⁻¹, which can be assigned to mode M vibrations: MA rotation, MA wagging, and symmetric MA–MA stretch, in good agreement with a cross correlation between isolated MAs and periodic calculations.¹⁶ This agreement can partly be attributed to the small difference between the extended crystals as a corner-sharing octahedral framework and the isolated clusters. Care has to be taken, however, since the cluster model emulates the crystal in only one direction, and only these vibrations should be taken as representative of the crystalline system. As mentioned earlier, also periodic calculations find vibrations at low wavenumbers, 62 and 94 cm⁻¹. The low wavenumbers are in the same region as our calculated values and compare favorably to their experimental data, but they also found the strongest intensity at 119 cm⁻¹ on meso-MAPbI₃, not assigned to the Pb–I system.^{30,31}

For our system we find a peak at 145 (143) and stronger bands at 167 (149, 154, and 156) and 217 (very weak theoretical transition) cm⁻¹ below 250 cm⁻¹ that are related to the MA cation, as assigned in Table s2. Comparing this to the Raman spectrum of MAPbI₂Cl shows that the mode B as peak "b'" shows peak shift to lower intensity. This phenomenon is significantly correlated with the results of XRD patterns and PL spectra, which show more disordered inorganic frameworks. According to Coslovich *et al.*,³² higher Raman activities have been observed to increase the electron–phonon interaction between the central cationic metal and anionic oxygen. It was suggested to decrease the low-energy electronic conductivity on superconductive material in inorganic perovskites. In our study, we can consider this effect for MAPbI₃ and the sub-MAPbI₃ crystal in MAPbI₂Cl on modes A and C in comparison. If the same reasoning would hold in the MAPbI₂Cl sample, the observed enhancement is seen of two local electron–phonon interactions in modes A and C but also a slightly decreased electron–phonon interaction in mode B compared to the MAPbI₃ sample. In particular, a significantly different Raman intensity is distinguished in the range 136–150 cm⁻¹ that shows 1.3 times higher Raman intensity in the MAPbI₃ sample at 143 cm⁻¹ compared to what the MAPbI₂Cl sample shows at 145 cm⁻¹, as seen in Figure 4. From the previous assignment in Table s2, this would correspond to the rotation of the MA unit around its own axis and also close to the MA wagging. As the laser can affect the composition of materials with any volatile organic compound, very low laser intensities were instead used (<0.01 mW) in Figure 4h and i. Here the intensity is up to 7 times higher at ~145 cm⁻¹ for the MAPbI₃ sample compared to MAPbI₂Cl. The Stokes line in Raman measurements comes from the losses of the electromagnetic energy in the laser light to an excited vibration level in the bond where the intensity comes from the change in polarizability of the electron cloud during the vibration. The laser used for the Raman measurements on the OMHPs electronically excites the material, and we thus have a substantial resonance Raman effect enhancing the signal due to the electron cloud polarization from the excitation in the incoming

TABLE 1. Charge Orbital Transition of Three Different Halide-Substituted OMHPs Such as 2MAPbX_6 Clusters by DFT Calculations

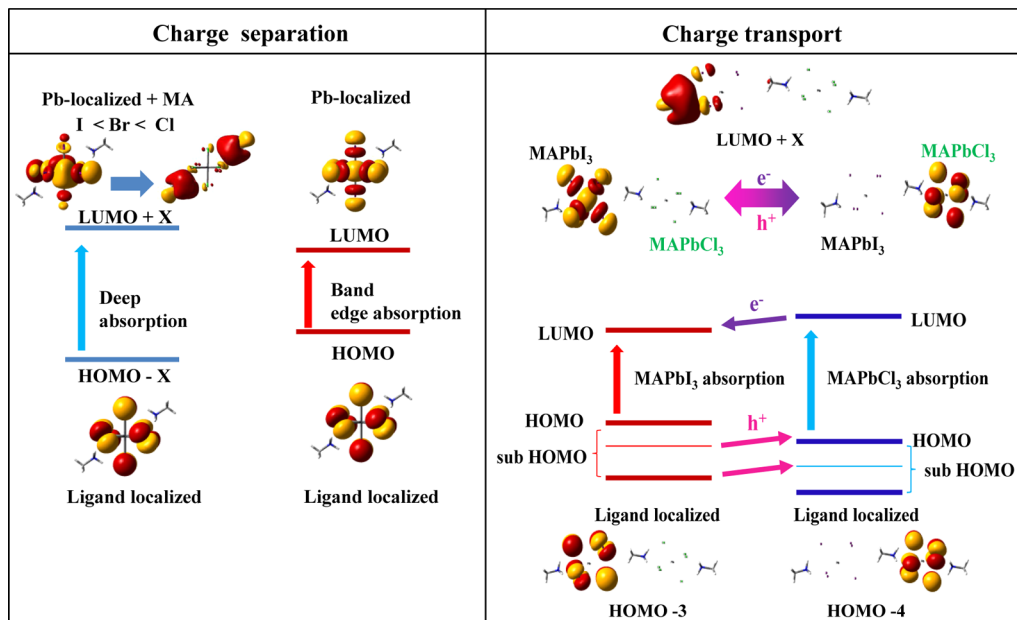
	HOMO	LUMO	LUMO+1	LUMO+2
2MAPbI_6				
2MAPBr_6				
2MAPCl_6				

electromagnetic field. During illumination, the perturbation Hamiltonian between the initial and final states, H_{if}' , can be expressed in terms of how the incoming spatial electromagnetic field, $E(r)$, induces a displacement of the electron and thus in terms of the transition dipole moment, μ_{if} , as in eq 1,

$$H_{if}' = -\frac{i\omega A}{m_0} \int \Psi_i^* e r \Psi_f d^3 r = -\frac{1}{m_0} \mu_{if}' E_0 \quad (1)$$

where A is the incoming spatial field, ω is the angular frequency, Ψ_i^* is the complex conjugate wave function of the initial state, Ψ_f is the accepting wave function for the virtual state, m_0 is the mass of an electron, e is the elementary charge of an electron, r is the displacement, and E_0 is the polarization field in the direction of the dipole. Since the expectation value of the displacement for a small interaction volume is small compared to the wavelength, one can utilize the dipole approximation and thus the assumption of the independence of the spatial field $A(r)$ for a small displacement r . The disappearance of the feature at 143 cm^{-1} during resonance excitation at 532 nm then implies that the initial and final state polarization disappears for the corresponding Raman rotation/wagging in the MA cation. Note that the initial (*i*) and final states (*f*) are not the HOMO–LUMO (or valence band–conduction band) transition that is expected to occur at lower wavelengths (790 nm) but excitations deeper in the absorption spectrum (532 nm) and also where the devices show high IPCE values. The remarkable difference at $143\text{--}145 \text{ cm}^{-1}$ between MAPb_3 and MAPb_2Cl samples seems to correlate with local charge transfer yield. The implication for such an effect on the local

charge localization can be investigated in the OMHPs by DFT simulation. In previous studies,^{33,34} the highest occupied molecular orbital (HOMO) and the lowest unoccupied molecular orbital (LUMO) are demonstrated on a cluster level in PbI_6 for MAPbI_3 . In Table 1, our DFT simulation results for unit clusters of OMHPs display the transitions of charges from the HOMO to LUMO (with LUMO+1 and LUMO+2). The HOMO of 2MAPbI_6 indicates an $\text{I} 5p \pi$ -bonding orbital, and its LUMO, LUMO+1, and LUMO+2 are decomposed to “ $\text{Pb}(6s)\text{--I}(5p)$ ” σ -antibonding, “ $\text{Pb}(6p)\text{--I}(5p)$ ” σ -antibonding, and “ $\text{Pb}(6s)\text{--I}(5p)$ ” σ -antibonding orbitals. The observation of 7 times lower intensity for the 143 cm^{-1} mode in the case of the MAPb_2Cl sample corresponds to a loss of polarization on mode M (m in experiments) of internal MAPb_3 . One reasonable explanation would be a photoexcited state that cannot change its polarizability as easily, such as an MA cation radical or neutral MA molecule. This state can then play an important role as an organic cation charge stabilizer or a neutral dipolar molecule in the cage of the inorganic framework. In a previous study by Frost *et al.*,³⁴ the importance of macroscopic static dielectric response and dipole order of various organic cations for OMHPs was investigated by DFT calculation but not in view of a MA radical but instead the dipole effect. A much improved charge stabilization in layered zirconium phosphonate-viologen compounds (ZrPV(X) , with $X = \text{Br}, \text{Cl}$) has previously been suggested to be via the creation of a phosphonate-viologen radical cation.³⁵ Also here, the effect was much improved when going from a heavier halogen to a lighter halogen, suggested to be an effect of delocalization of the



Scheme 2. Schematic picture of the charge localization (left) and charge transfer processes (right).

523 charges onto the organic cation and shielding from
524 molecular oxygen.
525 In order to investigate the improved possibility of
526 MA stabilizing a charge at higher excitations, DFT
527 calculations were performed. The HOMO, LUMO,
528 LUMO+1, and LUMO+2 of a dipolar canceling and
529 stoichiometric cluster of (MA)₂PbI₆, (MA)₂PbBr₆, and
530 (MA)₂PbCl₆ are shown in Table 1 and Scheme 2 (left
531 panel). For all the clusters, a ligand-to-metal charge
532 transfer is seen for the HOMO–LUMO transition, where
533 the initial localization on the iodine in the HOMO state
534 is significantly transferred to the Pb central unit in
535 the LUMO state. From the discussion above on the reso-
536 nance Raman effect at 532 nm exciting the material to
537 higher energy levels than the LUMO, we need to look
538 at higher unoccupied states. Looking at LUMO+2, we
539 see no localization on the MA cations in the (MA)₂PbI₆
540 but some partial occupation for (MA)₂PbBr₆ and a very
541 clear localization on the MA cation for (MA)₂PbCl₆. The
542 DFT calculations thus give strong support for improved
543 charge localization at the MA cation for high unoccu-
544 pied states in the series I → Br → Cl. If the MA cation
545 also is more liberated to rotate in this state due to
546 charge neutrality, this would also improve its possibili-
547 ties to align and work better in forming a ferroelectric
548 system. Consequently, Br (or Cl) atom substituted
549 MAPbX₆ can thus enhance the ferroelectric properties
550 caused by ordering of the MA molecule due to the
551 much improved freedom to rotate for a neutral dipolar
552 molecule compared to its more positively charged
553 analogue in 2MAPbI₆. An important but maybe not
554 obvious effect is also that the dipole of the neutral
555 MA is stronger than the positively charged analogue
556 MA⁺. DFT calculations for isolated molecules at
557 the B3LYP/6-311G(d,p) level show a dipole of 2.22 D

for the positively charged MA⁺ and 3.02 D for the neu-
558 tral MA.
559

The external quantum efficiency can be described
560 by factorization of the incident-photon-to-current-
561 efficiency (IPCE), as in eq 2.
562

$$\text{IPCE}(\lambda) = \text{LHE}(\lambda) \times \Phi_{\text{sep}}(\lambda) \times \Phi_{\text{trans}}(\lambda) \times \eta_{\text{coll}} \quad (2)$$

where λ is the wavelength of the light, LHE is the light-
563 harvesting efficiency, Φ_{sep} is the quantum efficiency
564 for charge separation, Φ_{trans} is the quantum efficiency
565 for transport, and η_{coll} is the charge collection effi-
566 ciency of the charges at the contact materials. The
567 results presented here give support for a excitation-
568 dependent charge separation mechanism where
569 $\Phi_{\text{sep}}(\lambda_{\text{band-edge}})$ is dominated by halogen-to-lead
570 charge separation, whereas absorption at higher
571 excitation energies $\Phi_{\text{sep}}(\lambda_{\text{deep-abs}})$ show a successively
572 larger influence of halogen-to-cation charge transfer in
573 the series I → Br → Cl.
574

As discussed above, liberation of the MA cation and
575 also the higher dipole of a neutral MA in the excited
576 state would also have consequences for the possibility
577 to align the MA dipoles and thus also for local fields
578 affecting the charge transport of the steady-state
579 current flowing through the solar cell device. To
580 investigate this effect in an idealized model system,
581 we performed calculations on two model systems with
582 extended clusters, AMPbI₆-MA-PbI₆-AM and AM-PbCl₆-
583 MA-PbI₆-AM, with two MA cations having a dipole-
584 canceling effect on the first cluster and two ordered
585 dipoles in a row for the second cluster, depicted in
586 Table s4. The ligand-to-metal charge transfer is now
587 instead from the ligands in the initial cluster to a more
588 metal-centered state in the neighboring cluster. As
589 expected, the alignment of the MA dipole improves
590

the hopping mechanism in the direction of the dipole. In a solar cell working at full illumination and with light that also includes higher wavelengths than the limiting HOMO–LUMO transition, higher states are of course active both in the charge separation mechanism (as we have discussed earlier) and for the transport up to LUMO+2. MA does not seem to contribute to a viable path for charge transport, but for LUMO+5 we see accepting orbitals also on the MA cations, as seen also for the smaller clusters. The absorption edge transition charge separation and transport mechanisms thus seem to be dominated by the ligand-to-metal transitions and hopping between the clusters mediated in the direction of the MA dipole, whereas at lower wavelengths in the region of the high IPCE values, the stabilization of the charges at the MA cation seems to be more important. Also the lower states, HOMO–1, HOMO–2, etc., are important, as the electrons are excited at higher energies than the HOMO–LUMO limiting transition. The initial creation of a hole would then be described by the lack of electron density previously found in the state. After some time under pulsed light or very weak light intensity, bond-length relaxation with the new electron configuration would occur and eventually higher state electrons would relax into the lower states and restore the original bond-length distribution. Under solar illumination and full working conditions, however, the low states, as well as the higher states, will continuously be excited and a steady-state condition of empty lower states can form a hole-conductive pathway in the system. The electron-conducting states will predominantly be described by the virtual orbitals, and the hole-conducting states by the empty HOMO and lower lying states. In Table S4, the initial localizations of electrons that can be lost under excitation are depicted. The electron localization clearly shows that steady-state excitation of these states will exclusively take part with localization at the iodine-ligand positions that are percolating in the crystalline OMHPs via sharing of iodine. This can be contrasted with the electron transport that is predominantly occurring via more Pb-localized states close to the HOMO–LUMO transition and localized at the MA cations for higher transitions in the absorption spectra. The mechanism ruling the quantum efficiency for transport, $\Phi_{\text{trans}}(\lambda)$, in eq 2, thus also reveals an energy dependence.

We especially observe the notable local HOMO–HOMO transition possible between PbI_6 and PbCl_6 units below the HOMO–1 for a cluster of MA- PbI_6 -MA- PbCl_6 -MA in Table S4. This electron transition can consequently be assisting charge transfer with local charge pumping processes via higher and lower sub-HOMO states and, as such, affect the LHE factor in eq 2.

The photovoltaic properties of OMHPs with nominal compositions MAPbI_3 , MAPbI_2Br , and MAPbI_2Cl were also tested. SEM cross sections of fabricated thin-film

solar cell devices are shown in Figure 5. The highly crystalline nature of the MAPbI_2Cl material is clear. In comparison, MAPbI_3 and MAPbI_2Br layers look much more smooth and amorphous. The solar cell performance was best for MAPbI_2Cl devices, as is evident from the J – V curves under 1 sun illumination in Figure 6a. The solar cell efficiencies were 5.8% for MAPbI_3 (FF: 0.50, V_{oc} : 0.77 V, J_{sc} : 15.0 mA/cm²), 3.2% for MAPbI_2Br (FF: 0.43, V_{oc} : 0.80 V, J_{sc} : 9.3 mA/cm²), and 10.0% for MAPbI_2Cl (FF: 0.50, V_{oc} : 1.0 V, J_{sc} : 20.4 mA/cm²). Incident photon to photocurrent conversion efficiency spectra (see Figure 6b) also show the best performance for MAPbI_2Cl , with IPCE values reaching nearly 85%. The integrated photocurrent values (Figure 6b) are calculated from the IPCE spectra and are in good agreement with the experimental short-circuit current densities measured in the solar simulator. The extrapolated onset wavelength from the IPCE spectrum is 800 nm for MAPbI_3 , 785 nm for MAPbI_2Cl , and 720 nm for MAPbI_2Br , in accordance with the optical band gaps in Figure 6c. The MAPbI_2Br solar cell showed the lowest current density among the samples due to the lowest light-harvesting efficiency from UV-vis spectra and the lowest bulk conductivity. On the other hand, it indicates the possibility for higher V_{oc} from longer charge carrier lifetime τ from PL intensity (and higher local polarizability) than the corresponding MAPbI_3 as mentioned above. The MAPbI_2Cl solar cell showed the highest V_{oc} and J_{sc} as 1.0 V and 20.40 mA/cm², respectively, which can be attributed to the longest charge carrier lifetime and a high ferroelectric property and thus an enhanced local conductivity caused by the stabilization of charges of MA cations as discussed above. All solar cell performances are in good agreement with our more detailed results on the effect of local charge stabilization at the MA in the series I > Br > Cl in OMHPs and its effects on the ordering of the MA cation.

Interestingly, MAPbI_2Cl has a dip as zone A in the IPCE spectrum below 430 nm in Figure 6c, which can be attributed to competitive light absorption by the MAPbCl_3 crystals in this material in Figure 6d, which apparently does lead to low photocurrent. On the other hand, the increase in the IPCE curve as zone B is observed and is an interesting phenomenon. We fortunately have the results on the charge transfer mechanism in the DFT calculation above. The existence of a PbCl_6 unit in connection to a PbI_6 unit would allow for a charge pumping property at a low HOMO level. This would lead to an improved charge excitation from the rising sub-HOMO level to the LUMO. This process would then explain the huge difference of IPCE at 600–800 nm wavelength as zone B and help to enhance the local charge carrier lifetime (see Scheme 2 (right panel)); the normalized PL spectra for MAPbCl_3 and MAPbI_2Cl with the sum of PL spectra are summarized in Figure 6d. We thus find a possible charge-pumping

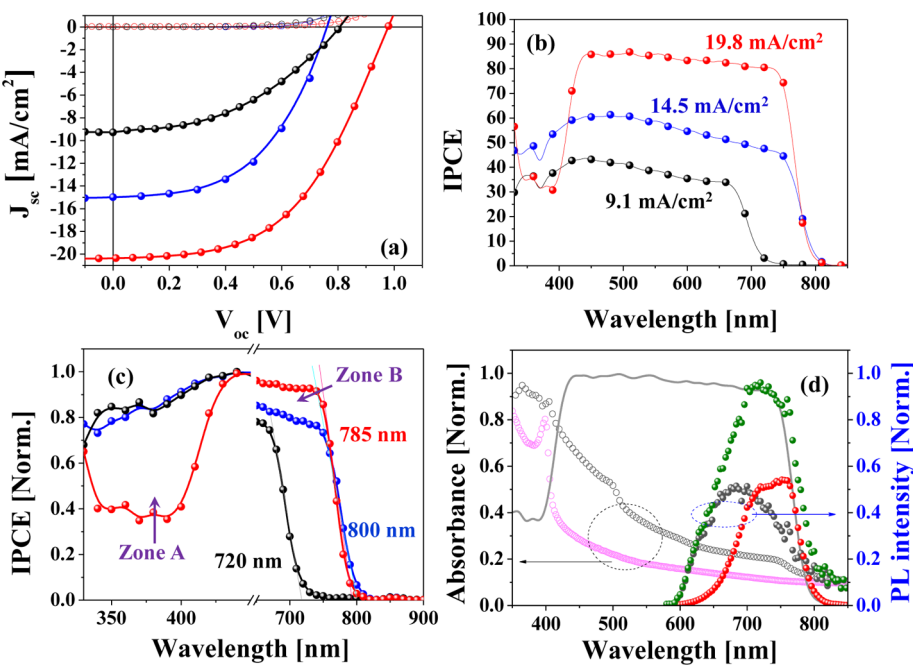


Figure 6. Summarized solar cell performances: (a) $J-V$ characterization, (b) IPCE curves, (c) normalized IPCE curves for MAPbI_3 (blue solid line), MAPbI_2Br (black solid line), and MAPbI_2Cl (red solid line) utilized solar cell devices. (d) Normalized UV-vis and PL spectra for MAPbCl_3 (pink and red round symbols) and MAPbI_2Cl (dark gray round symbols). Sum of PL spectra (green round symbols) from two given samples; gray solid line is an IPCE curve of MAPbI_2Cl .

processes between MAPbCl_3 (insulator) and MAPbI_3 (semiconductor) subcrystallites within MAPbI_2Cl . To further analyze this and the role of charge pumping requires more detailed experiments and is an interesting scope for future work.

CONCLUSIONS

In summary, we observe a change in the local structure of I, Br, and Cl in the OMHPs from XRD and Raman measurements. MAPbI_2Br -based solar cells show higher V_{oc} than MAPbI_3 , and this can be from the effect of enhanced antiferroelectric properties, as indicated by a 3 times enhancement of the charge carrier lifetime as measured with PL compared to MAPbI_3 . Here we have investigated MAPbI_2Cl in more detail and show two subcrystallites, MAPbI_3 and MAPbCl_3 . These crystallites show a change in the local structure compared to the MAPbI_3 reference sample. The disordered octahedral framework of MAPbI_3 with a liberated MA cation has a remarkably longer charge lifetime than MAPbI_3 with an ordered MA cation. Furthermore, the disordered MAPbI_3 induced by addition of chlorine shows an up to 7 times lower change in polarizability and thus a deactivated mode M (m). This can be understood by an increased charge localization

on the MA cation upon excitation and thus improves the possibilities for dipole alignment in response to a local field and thus enhanced ferroelectric properties. Results from DFT calculations on model clusters support this picture and show an excitation energy dependent mechanism for the charge transfer. The near-band-edge transition is dominated by an iodide to lead transition (ligand-to-metal), whereas the higher virtual states show a successively higher localization on the MA cation in the series I–Br–Cl. The lower sub-HOMO states exclusively show iodide (ligand) and chloride (ligand) localized states in close range, making a sub-HOMO pumping process possible, which can explain the increasing IPCE in the 600–800 nm range for MAPbI_2Cl in comparison to MAPbI_3 . The material properties analyzed are well justified by the device performance, showing 1.7 times higher PCE with inclusion of chlorine compared to that of MAPbI_3 solar cells. Here, we have presented an excitation-dependent mechanistic view of the heterojunction charge localization and transfer between MAPbI_3 and MAPbCl_3 within local MAPbI_2Cl crystallites, which can possibly open up a new understanding of the nature of OMHP materials in hybrid thin-film solar cell applications.

METHODS

Material Preparation. Organic lead halide hybrid perovskites (OMHPs) were prepared by a low-temperature melting method from different precursor solutions. The starting materials were

PbI_2 (purity 99%, Sigma-Aldrich), methylamine solution (40% in methanol, TCI), hydrochloric acid (37 wt % in water, Aldrich), hydroiodic acid (57 wt % in water, Aldrich), and hydrobromic acid (48 wt % in water, Aldrich). $\text{CH}_3\text{NH}_3\text{Cl}$, $\text{CH}_3\text{NH}_3\text{Br}$, and

763 $\text{CH}_3\text{NH}_3\text{I}$ were synthesized by mixing hydrogen halide acids
 764 with methylamine solution in equal molar ratio in a 250 mL
 765 round-bottom flask at 0 °C for 2 h with stirring. The precipitate
 766 was recovered by evaporation at 50 °C for 1 h. The products
 767 were washed in diethyl ether by stirring the solution for 30 min,
 768 which was repeated three times, and then finally dried at 60 °C
 769 in a vacuum oven for 24 h. The obtained $\text{CH}_3\text{NH}_3\text{Cl}$, $\text{CH}_3\text{NH}_3\text{Br}$,
 770 or $\text{CH}_3\text{NH}_3\text{I}$ salts were mixed with PbI_2 (purity 98.0% Sigma-
 771 Aldrich), PbBr_2 (purity 98.0% Sigma-Aldrich), or PbCl_2 (purity
 772 98.0%, Sigma-Aldrich) in a 1:1 molar ratio in a mixture of
 773 dimethylformamide (DMF) and dimethyl sulfoxide (DMSO)
 774 (7:3 = vol/vol) at 70 °C for 2 h. The concentration of the resulting
 775 precursor is 1.5 M. The OMHP precursors of MAPbI_3 , MAPbBr_3 ,
 776 MAPbCl_3 , MAPbI_2Br , and MAPbI_2Cl were deposited on different
 777 substrates by a spin-coating method at 1500 rpm (± 25 rpm) for
 778 20 s. After spin-coating OMHPs precursor films were annealed
 779 on a hot plate at 100 °C for 35 min under dry air conditions
 780 (relative humidity below 30%). Mesoporous TiO_2 films were
 781 prepared by diluting TiO_2 paste (Dyesol, DSL 30 NRD) with
 782 2-propanol (1:4 by weight) and spin-coating at 3000 rpm for
 783 20 s, resulting in films of 450 nm (± 50 nm) thickness after
 784 annealing at 450 °C.

785 **X-ray Diffraction.** The crystallographic properties of the per-
 786 ovskite films deposited on mesoporous TiO_2 -coated micro-
 787 scopic slides or bare microscopic slides were investigated
 788 using XRD with a Siemens D5000 diffractometer apparatus with
 789 a Kristaller-Flex 710D X-ray generator using Cu K α 1 radiation
 790 (0.154 056 2 nm, fine-focus sealed tube source with a Gobel
 791 mirror) at room temperature. The Diffrac Plus XRD commander
 792 program was used to control the instrument. The instrument
 793 was set in "detector scan" mode, and the acquisition was done
 794 in $\theta \approx 2\theta$ mode for every 0.02° increment over the Bragg angle
 795 range of 10–60°. The XRD patterns were fitted by the X'pert
 796 highScore program.

797 **Scanning Electron Microscopy (SEM).** SEM was performed on a
 798 Zeiss (Gemini 1550) microscope having a field emission electron
 799 source and an in-lens detector for secondary electrons. Top
 800 view images and cross sections of solar cell devices were
 801 recorded using a high tension of 5 kV. OMHPs were coated on
 802 ITO glass substrates for top view images.

803 **Raman Measurements.** Raman spectra were measured with a
 804 Renishaw InVia Raman spectrometer with 1 cm^{-1} resolution
 805 using a frequency-doubled YAG laser (532 nm) and an 1800
 806 lines/mm grating. A 50× objective was used and gave a laser
 807 spot with 3–5 μm diameter with 0.01–1 mW intensity on the
 808 sample depending on measurement mode. A notch filter was
 809 used for the Rayleigh (Plasma) line of the 532 nm laser and a cut
 810 filter 10 cm^{-1} into the Stokes part of the spectra. For each
 811 sample, 50 spectra were recorded in the range 10–400 cm^{-1}
 812 with no apparent change in the spectra during the cycles.
 813 OMHPs were coated on microscope glass substrates.

814 **Steady-State Emission Measurements.** Standard steady-state
 815 emission spectra were obtained on a Fluorolog-3 instrument
 816 (Horiba Jobin Yvon) equipped with double-grating excitation
 817 and emission monochromators and a 450 W Xe lamp as a light
 818 source. The emission spectra were corrected for the spectral
 819 sensitivity of the detection system by using a calibration file of
 820 the detector response. Front-face illumination (30° with respect
 821 to the incident beam) was used to minimize inner-filter effects.
 822 Excitation was done at 610 nm. OMHPs were coated on micro-
 823 scope glass substrates.

824 **UV–Vis–NIR Spectra Measurements.** UV–visible–NIR absorption
 825 spectra were recorded using a Cary 5000 UV–vis–
 826 NIR spectrophotometer (Varian, photometric accuracy is
 827 <0.000 25 Abs, photometric range is 8 Abs). OMHPs were coated
 828 on microscope glass substrates, and the microscope glass was
 829 used as reference.

830 **Calculations.** The density functional theory calculations were
 831 performed within the Gaussian09 package³⁶ using the hybrid
 832 functional B3LYP with the 6-311G(d,p) basis set and the Stutt-
 833 gart-Dresden effective core potentials (ECP) for the heavy
 834 elements. The convergence criterion was set to 10^{-8} hartrees,
 835 and quantum mechanical linear response calculations were
 836 used in subsequent calculations to obtain the theoretical
 837 Raman spectra.

Fabrication and Performance of Measurement for Solar Cell Devices. 838
Fabrication of Solar Cell Devices. 839
 Solar cells were prepared for 840
 OMHPs with nominal compositions MAPbI_3 , MAPbI_2Br , and 841
 MAPbI_2Cl . Fluorine-doped tin oxide (FTO)-coated glass 842
 (Pilkington TEC 15, 15 Ω/\square) was patterned using an etching 843
 process with Zn powder and 2 M HCl diluted in water. Compact 844
 TiO_2 layers (thickness 30–60 nm) were deposited on the FTO 845
 substrate by spray pyrolysis on a hot plate (kept at 500–550 °C).³⁵ 846
 The prepared TiO_2 precursor was coated by a spin-caster at 847
 4000 rpm (± 30 rpm) for 20 s and annealed on a hot plate at 848
 500 °C for 30 min. The OMHP precursor was also deposited by a 849
 spin-coater at 1250 rpm (± 25 rpm) for 20 s and annealed at 850
 135–145 °C for 30–40 min in a drybox at 20–40% humidity. The 851
 hole transporter spiro-MeOTAD was deposited by spin-coating at 852
 1500 rpm for 20 s as described before (see ref 15). Finally, 150 nm 853
 thick silver electrodes were deposited on top of the devices by 854
 thermal evaporation at $\sim 10^{-6}$ bar, through a shadow mask. 855
Power Conversion Efficiency. 856
 A Newport solar simulator (model 91160), giving light with AM 1.5 G spectral distribution, 857
 was calibrated using a certified reference solar cell (Fraunhofer 858
 ISE) to an intensity of 1000 W m^{-2} . The electrical data were 859
 recorded with a computer-controlled digital source-meter (Keithley 860
 model 2400) with the scan direction from the open-circuit to short-circuit at a scan rate of 800–1250 mV s^{-1} .³⁸ The 861
 solar cells were masked during the measurement with an 862
 aperture area of 0.126 cm^2 (round type of mask).³⁹ The 863
Incident Photon to Current Conversion Efficiency. 864
 The IPCE spectra were recorded with a computer-controlled setup 865
 comprising a xenon lamp (Spectral Products, ASB-XE-175), a 866
 monochromator (Spectral Products, CM110), and a Keithley 867
 multimeter (model 2700). The setup was calibrated with a 868
 certified silicon solar cell (Fraunhofer ISE) prior to the 869
 measurements. All DSCs were illuminated from the WE side with an 870
 aperture area of 0.126 cm^2 (round type of mask) using a black 871
 mask. The MAPbI_3 -deposited solar cell was measured without 872
 bias light, and MAPbI_2Br - and MAPbI_2Cl -utilizing solar cells 873
 were measured under each different bias light intensity of 0.05 874
 and 0.09 sun. 875

Conflict of Interest: The authors declare no competing financial interest. 876
 877

Acknowledgment. We thank the Swedish Energy Agency, 878
 the STAndUP for Energy Program, the Swedish Research Council 879
 (VR), the Göran Gustafsson Foundation, and the Knut and Alice 880
 Wallenberg Foundation for financial support. T.E. thanks the 881
 Ångpanneföreningens Research Foundation for financial support. 882
 B-w.P. thanks the members of the Korea Swedish Scientists and 883
 Engineers Association (KSSEA) for support and thanks, in particular, 884
 Taeja Kim-Björklund, chairman of the KSSEA and Korean 885
 Association in Sweden. Further thanks go to Mr. Seockjeong 886
 Eom, Ambassador in the Embassy of the Republic of Korea in 887
 Sweden. B-w.P. prepared the starting materials, composed the 888
 OMHPs, fabricated the solar cell devices, analyzed the data from 889
 crystallography, PL spectra, Raman spectra, DFT calculations, 890
 and all solar cell properties (J – V and IPCE curves), and participated 891
 in writing the manuscript; S.M.J. supported the fabrication 892
 of the solar cell devices and the preparation of OMHPs and 893
 participated in writing the manuscript; X.Z. performed the SEM 894
 experiments; A.H. guided the work and edited the manuscript; 895
 G.B. edited the manuscript and supervised; T.E. carried out the 896
 DFT calculations and Raman investigations, participated in 897
 writing the manuscript, and guided the work. 898

Supporting Information Available: Additional plots of the 899
 experimental Raman and PL spectra, XRD data, calculated 900
 Raman spectra, super-LUMO and sub-HOMO orbital localizations, 901
 and solar cell performances for many measurements on 902
 OMHP devices with error bars can be found in the Supporting 903
 Information. This material is available free of charge via the 904
 Internet at <http://pubs.acs.org>. 905

REFERENCES AND NOTES

- Weber, D. $\text{CH}_3\text{NH}_3\text{SnBr}_{x}\text{I}_{3-x}$ ($x = 0–3$), a Sn(II)-System with Cubic Perovskite Structure. *Z. Naturforsch.* **1978**, 33b, 862–865. 906
 907
 908

- 909 2. Weber, D. $\text{CH}_3\text{NH}_3\text{PbX}_3$, a Pb(II)-System with Cubic Perovskite Structure. *Z. Naturforsch.* **1978**, *33b*, 1443–1445.
 910 3. Kojima, A.; Teshima, K.; Shirai, Y.; Miyasaka, T. Organometal Halide Perovskites as Visible-Light Sensitizers for Photovoltaic Cells. *J. Am. Chem. Soc.* **2009**, *131*, 6050–6051.
 911 4. Kim, H.-S.; Lee, C.-R.; Im, J.-H.; Lee, K.-B.; Moehl, T.; Marchioro, A.; Moon, S.-J.; Humphry-Baker, R.; Yum, J.-H.; Moser, J. E.; et al. Lead Iodide Perovskite Sensitized All-Solid-State Submicron Thin Film Mesoscopic Solar Cell with Efficiency Exceeding 9%. *Sci. Rep.* **2012**, *2*, 591.
 912 5. Lee, M. M.; Teuscher, J.; Miyasaka, T.; Murakami, T. N.; Snaith, H. J. Efficient Hybrid Solar Cells Based on Mesosuperstructured Organometal Halide Perovskites. *Science* **2012**, *338*, 643–647.
 913 6. Im, J.-H.; Lee, C.-R.; Lee, J.-W.; Park, S.-W.; Park, N.-G. 6.5% Efficient Perovskite Quantum-Dot-Sensitized Solar Cell. *Nanoscale* **2011**, *3*, 4088–4093.
 914 7. Jeon, N. J.; Noh, J. H.; Kim, Y. C.; Yang, W. S.; Ryu, S.; Seok, S. I. Solvent Engineering for High-Performance Inorganic–Organic Hybrid Perovskite Solar Cells. *Nat. Mater.* **2014**, *13*, 897–903.
 915 8. Burschka, J.; Pellet, N.; Moon, S.-J.; Humphry-Baker, R.; Gao, P.; Nazeeruddin, M. K.; Grätzel, M. Sequential Deposition as a Route to High-Performance Perovskite-Sensitized Solar Cells. *Nature* **2013**, *499*, 316–319.
 916 9. Liu, M.; Johnston, M. B.; Snaith, H. J. Efficient Planar Heterojunction Perovskite Solar Cells by Vapour Deposition. *Nature* **2013**, *501*, 395–399.
 917 10. NREL. The Chart of Solar Cell Efficiency, http://www.nrel.gov/ncpv/images/efficiency_chart.jpg.
 918 11. Noh, J. H.; Im, S. H.; Heo, J. H.; Mandal, T. N.; Seok, S. I. Chemical Management for Colorful, Efficient, and Stable Inorganic–Organic Hybrid Nanostructured Solar Cells. *Nano Lett.* **2013**, *13*, 1764–1769.
 919 12. Zhu, K.; Zhao, Y. $\text{CH}_3\text{NH}_3\text{Cl}$ -Assisted One-Step Solution Growth of $\text{CH}_3\text{NH}_3\text{PbI}_3$: Structure, Charge–Carrier Dynamics, and Photovoltaic Properties of Perovskite Solar Cells. *J. Phys. Chem. C* **2014**, *118*, 9412–9418.
 920 13. Colella, S.; Mosconi, E.; Fedeli, P.; Listorti, A.; Gazzola, F.; Orlandi, F.; Ferro, P.; Besagni, T.; Rizzo, A.; Calestani, G.; et al. $\text{MAPbI}_{3-x}\text{Cl}_x$ Mixed Halide Perovskite for Hybrid Solar Cells: The Role of Chloride as Dopant on the Transport and Structural Properties. *Chem. Mater.* **2013**, *25*, 4613–4618.
 921 14. Eperon, G. E.; Stranks, S. D.; Menelaou, C.; Johnston, M. B.; Herz, L. M.; Snaith, H. J. Formamidinium Lead Trihalide: A Broadly Tunable Perovskite for Efficient Planar Heterojunction Solar Cells. *Energy Environ. Sci.* **2014**, *7*, 982–988.
 922 15. Mosconi, E.; Amat, A.; Nazeeruddin, M. K.; Grätzel, M.; Angelis, F. D. First-Principles Modeling of Mixed Halide Organometal Perovskites for Photovoltaic Applications. *J. Phys. Chem. C* **2013**, *117*, 13902–13913.
 923 16. Quarti, C.; Grancini, G.; Mosconi, E.; Bruno, P.; Ball, J. M.; Lee, M. M.; Snaith, H. J.; Petrozza, A.; Angelis, F. D. The Raman Spectrum of the $\text{CH}_3\text{NH}_3\text{PbI}_3$ Hybrid Perovskite: Interplay of Theory and Experiment. *J. Phys. Chem. Lett.* **2014**, *5*, 279–284.
 924 17. Park, B.-w.; Philippe, B.; Gustafsson, T.; Sveinbjörnsson, K.; Hagfeldt, A.; Johansson, E. M. J.; Boschloo, G. Enhanced Crystallinity in Organic-Inorganic Lead Halide Perovskites on Mesoporous TiO_2 via Disorder-Order Phase Transition. *Chem. Mater.* **2014**, *26*, 4466–4471.
 925 18. Chen, Q. i.; Zhou, H.; Song, T.-B.; Luo, S.; Hong, Z.; Duan, H.-S.; Dou, L.; Liu, Y.; Yang, Y. Controllable Self-Induced Passivation of Hybrid Lead Iodide Perovskites toward High Performance Solar Cells. *Nano Lett.* **2014**, *14*, 4158–4163.
 926 19. Frost, J. M.; Butler, K. T.; Brivio, F.; Hendon, C. H.; Schilfsgaarde, M.; Walsh, A. Atomistic Origins of High-Performance in Hybrid Halide Perovskite Solar Cells. *Nano Lett.* **2014**, *14*, 2584–2590.
 927 20. Eremets, M. I.; Takemura, K.; Yusa, H.; Golberg, D.; Bando, Y.; Blank, V. D.; Sato, Y.; Watanabe, K. Disordered State in First-Order Phase Transitions: Hexagonal-to-Cubic and Cubic-to-Hexagonal Transitions in Boron Nitride. *Phys. Rev. B* **1998**, *57*, 5655.
 928 21. Binder, K. Theory of First-Order Phase Transitions. *Rep. Prog. Phys.* **1987**, *50*, 783–859.
 929 22. Even, J.; Pedesseau, L.; Jancu, J.-M.; Katan, C. Importance of Spin–Orbit Coupling in Hybrid Organic/Inorganic Perovskites for Photovoltaic Applications. *J. Phys. Chem. Lett.* **2013**, *4*, 2999–3005.
 930 23. De Boer, W. D. A. M.; Timmerma, D.; Dohnalová, K.; Yassievich, I. N.; Zhang, H.; Buma, W. J.; Gregorkiewicz, T. Red Spectral Shift and Enhanced Quantum Efficiency in Phonon-Free Photoluminescence from Silicon Nanocrystals. *Nat. Nanotechnol.* **2010**, *5*, 878–884.
 931 24. Riboli, F.; Caselli, N.; Vignolini, S.; Intonti, F.; Vynck, K.; Barthelemy, P.; Gerardino, A.; Balet, L.; Li, L. H.; Fiore, A.; Gurioli, M.; Wiersma, D. S. Engineering of Light Confinement in Strongly Scattering Disordered Media. *Nat. Mater.* **2014**, *13*, 720–725.
 932 25. Sadhanala, A.; Deschler, F.; Thomas, T. H.; Dutton, S. E.; Goedel, K. C.; Hanusch, F. C.; Lai, M. L.; Steiner, U.; Bein, T.; Docampo, P.; et al. Preparation of Single-Phase Films of $\text{CH}_3\text{NH}_3\text{Pb}(\text{I}_{1-x}\text{Br}_x)_3$ with Sharp Optical Band Edges. *J. Phys. Chem. Lett.* **2014**, *5*, 2501–2505.
 933 26. Im, J.-H.; Chung, J.; Kim, S.-J.; Park, N.-G. Synthesis, Structure, and Photovoltaic Property of a Nanocrystalline 2H Perovskite-Type Novel Sensitizer ($\text{CH}_3\text{CH}_2\text{NH}_3\text{PbI}_3$). *Nanoscale Res. Lett.* **2012**, *7*, 353.
 934 27. Schreiber, J.; Hildebrandt, S.; Kircher, W.; Richter, T. Optical Investigations of Surface and Interface Properties at III-V Semiconductors. *Mater. Sci. Eng.* **1991**, *B9*, 31–35.
 935 28. Anicete-Santos, M.; Orhan, E.; de Maurera, M. A. M. A.; Simões, L. G. P.; Souza, A. G.; Pizani, P. S.; Leite, E. R.; Varela, J. A.; André, J.; Beltrán, A.; et al. Contribution of Structural Order-Disorder to the Green Photoluminescence of PbWO_4 . *Phys. Rev. B* **2007**, *75*, 165105.
 936 29. Blasse, G.; Corsmit, A. F. Electronic and Vibrational Spectra of Ordered Perovskites. *J. Solid State Chem.* **1973**, *6*, 513–518.
 937 30. Grancini, G.; Marras, S.; Prato, M.; Giannini, C.; Quarti, C.; Angelis, F. D.; Bastiani, M. D.; Eperon, G. E.; Snaith, H. J.; Manna, L.; et al. The Impact of the Crystallization Processes on the Structural and Optical Properties of Hybrid Perovskite Films for Photovoltaics. *J. Phys. Chem. Lett.* **2014**, *5*, 279–284.
 938 31. Capozzi, V.; Fontana, A.; Fontana, M. P.; Mariotto, G.; Montagna, M.; Viliani, G. Raman Scattering in PbI_2 . *Il Nuovo Cimento B* **1977**, *39*, 556–560.
 939 32. Coslovich, G.; Huber, B.; Lee, W.-S.; Chuang, Y.-D.; Zhu, Y.; Sasagawa, T.; Hussain, Z.; Bechtel, H. A.; Martin, M. C.; Shen, Z.-X.; et al. Ultrafast Charge Localization in a Stripe-Phase Nickelate. *Nat. Commun.* **2013**, *4*, 2643.
 940 33. Frost, J. M.; Butler, K. T.; Brivio, F.; Hendon, C. H.; Van Schilfgaarde, M.; Walsh, A. Atomistic Origins of High-Performance in Hybrid Halide Perovskite Solar Cells. *Nano Lett.* **2014**, *14*, 2584–2590.
 941 34. Umebayashi, T.; Asai, K.; Kondo, T.; Kakao, A. Electronic Structures of Lead Iodide Based Low-Dimensional Crystals. *Phys. Rev. B* **2003**, *67*, 155405.
 942 35. Vermeulen, L. A.; Thompson, M. E. Stable Photo-Induced Charge Separation in Layered Vologen Compounds. *Nature* **1992**, *358*, 656–658.
 943 36. Park, B.-w.; Yang, L.; Johansson, E. M. J.; Vlachopoulos, N.; Chams, A.; Perruchot, C.; Jouini, M.; Boschloo, G.; Hagfeldt, A. Neutral, Polaron, and Bipolaron States in PEDOT Prepared by Photoelectrochemical Polymerization and the Effect on Charge Generation Mechanism in the Solid-State Dye-Sensitized Solar Cell. *J. Phys. Chem. C* **2013**, *117*, 22484–22491.
 944 37. Frisch, M. J.; Trucks, G. W.; Schlegel, H. B.; Scuseria, G. E.; Robb, M. A.; Cheeseman, J. R.; Scalmani, G.; Barone, V.; Mennucci, B.; Petersson, G. A.; et al. *Gaussian 09*, Revision A.02; Gaussian, Inc.: Wallingford, CT, 2009.
 945 38. Sanchez, R. S.; Gonzalez-Pedro, V.; Lee, J.-W.; Park, N.-G.; Kang, Y. S.; Mora-Sero, I.; Bisquert, J. Slow Dynamic Processes in Lead Halide Perovskite Solar Cells. Characteristic Times and Hysteresis. *J. Phys. Chem. Lett.* **2014**, *5*, 2357–2363.
 946 984
 947 985
 948 986
 949 987
 950 988
 951 989
 952 990
 953 991
 954 992
 955 993
 956 994
 957 995
 958 996
 959 997
 960 998
 961 999
 962 1000
 963 1001
 964 1002
 965 1003
 966 1004
 967 1005
 968 1006
 969 1007
 970 1008
 971 1009
 972 1010
 973 1011
 974 1012
 975 1013
 976 1014
 977 1015
 978 1016
 979 1017
 980 1018
 981 1019
 982 1020
 983 1021
 984 1022
 985 1023
 986 1024
 987 1025
 988 1026
 989 1027
 990 1028
 991 1029
 992 1030
 993 1031
 994 1032
 995 1033
 996 1034
 997 1035
 998 1036
 999 1037
 1000 1038
 1001 1039
 1002 1040
 1003 1041
 1004 1042
 1005 1043
 1006 1044
 1007 1045
 1008 1046
 1009 1047
 1010 1048
 1011 1049
 1012 1050
 1013 1051
 1014 1052
 1015 1053
 1016 1054
 1017 1055
 1018 1056
 1019 1057

Supporting information

Resonance Raman and Excitation Energy Dependent Charge Transfer Mechanism in Halide Substituted Hybrid Perovskite Solar Cells

Byung-wook Park¹, Sagar M. Jain¹, Xiaoliang Zhang¹, Anders Hagfeldt^{1†}, Gerrit Boschloo^{1*}, Tomas Edvinsson^{2*}

¹Uppsala University, Department of Chemistry-Ångström Laboratory, Physical Chemistry, Box 523, SE 751 20 Uppsala, Sweden

²Uppsala University, Department of Chemistry-Ångström Laboratory, Inorganic Chemistry, Box 538, SE 751 21 Uppsala, Sweden

[†] Laboratory for Photomolecular Science (LSPM), Swiss Federal Institute of Technology at Lausanne (EPFL), CH-1015, Lausanne, Switzerland

*e-mail: gerriet.boschloo@kemi.uu.se, tomas.edvinsson@kemi.uu.se

Table s1. XRD peak positions, intensity, calculated lattice spacing and estimated grain sizes from XRD patterns in Figure 1(f).

OMHPs	Sub crystallite	Peak position (2θ)	Intensity (Counts)	FWHM (degree)	Grain size (nm)	d-space (nm)
MAPbI₃		14.14	123638	0.2880	27.79	0.6280
MAPbI₂Br		14.37	128385	0.3264	24.53	0.6159
MAPbI₂Cl	MAPbI₃	14.07	76009	0.3455	23.17	0.6289
	MAPbCl₃	15.53	53258	0.3331	24.07	0.5686
MAPbBr₃		14.92	167820	0.2967	27.00	0.5933
MAPbCl₃		15.57	216100	0.2967	24.07	0.5687

Table s2. Peak positions, intensity, calculated lattice spacing and estimated grain sizes from Raman spectra on model clusters in DFT calculation in Figure 4(a ~ g) and Figure s2.

Clusters	X	Mode A Asymmetric X-Z, X-Y, Y-Z [cm ⁻¹]	Mode B Asymmetric “breathing” [cm ⁻¹]	Mode C Symmetric “breathing” [cm ⁻¹]	Mode D Asymmetric Pb-Br(or Cl) stretch [cm ⁻¹]	Mode M			Mode N
						MA rotation [cm ⁻¹]	MA wagging [cm ⁻¹]	Symmetric MA-MA stretch [cm ⁻¹]	N-halide stretch via H [cm ⁻¹]
PbX₆	I	48	68	83	-	-	-	-	-
	Br	68	102	125	-	-	-	-	-
	Cl	112	186	215	-	-	-	-	-
2MAPbX₆	I	52, 54, 55	76, 77	89	-	143	149, 154	156	-
	Br	70, 71, 73	108, 109	132	-	144	157, 162	176	-
	Cl	104, 109, 110	212, 230	220	-	146	165, 166	202	-
	I₅Br	55, 56, 57	74, 78	91	118	146	150-160	192 with MA wagging	-
	I₄Br₂	58, 60, 65	78, 86	112	-	145	147	193 with MA wagging	-
	I₅Cl	45, 58	72, 76	86, 90, 94 Asymmetric	190	140	145-160	175 with MA wagging	240
	I₄Cl₂	47, 60	75, 82	89 Cl holding	185	138	143-145	180 with MA wagging	247

Table s3. Orbital localization for halogen substituted clusters

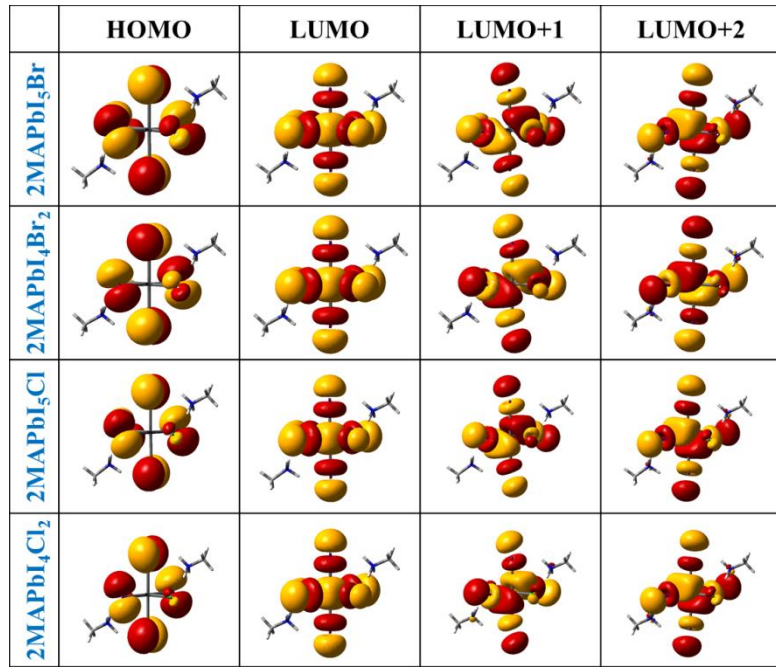
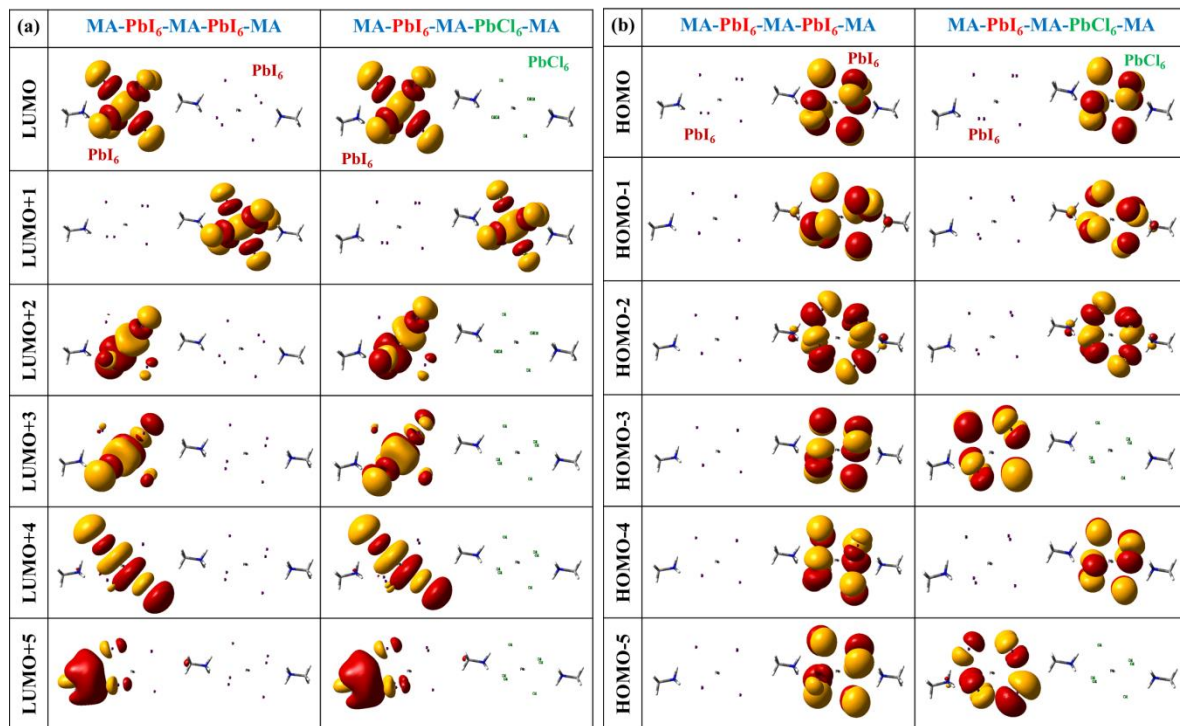


Table s4. Orbital localization for the suggested bi-molecules model clusters such as MA-PbI₆-MA-PbI₆-MA and MA-PbI₆-MA-PbCl₆-MA



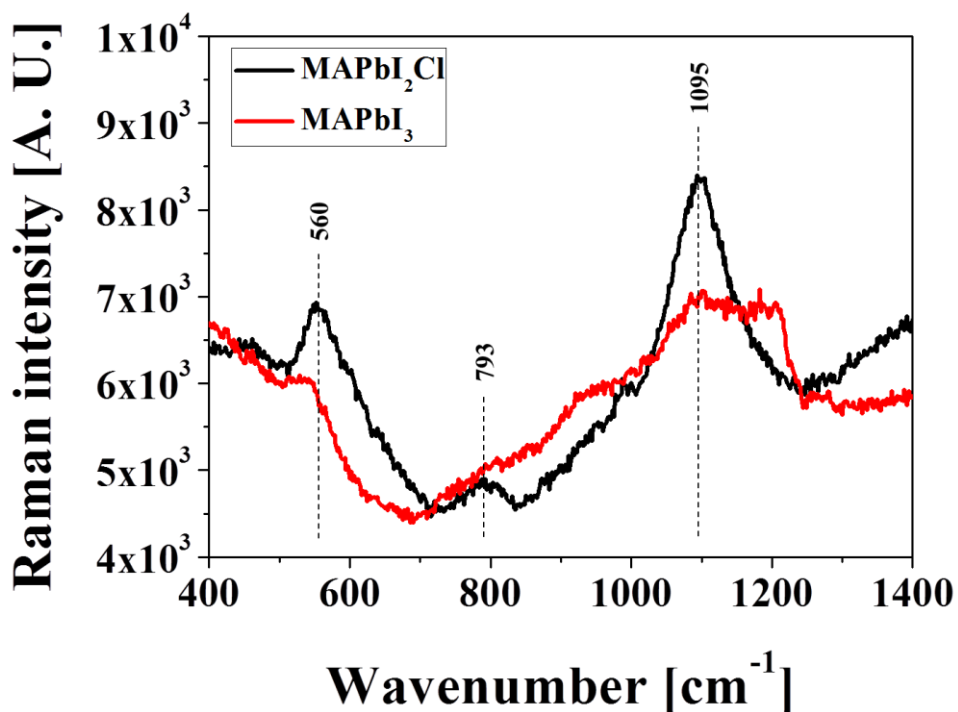


Figure S1. Raman spectra in the range of 400-1400 cm⁻¹ for MAPbI₂Cl and MAPbI₃.

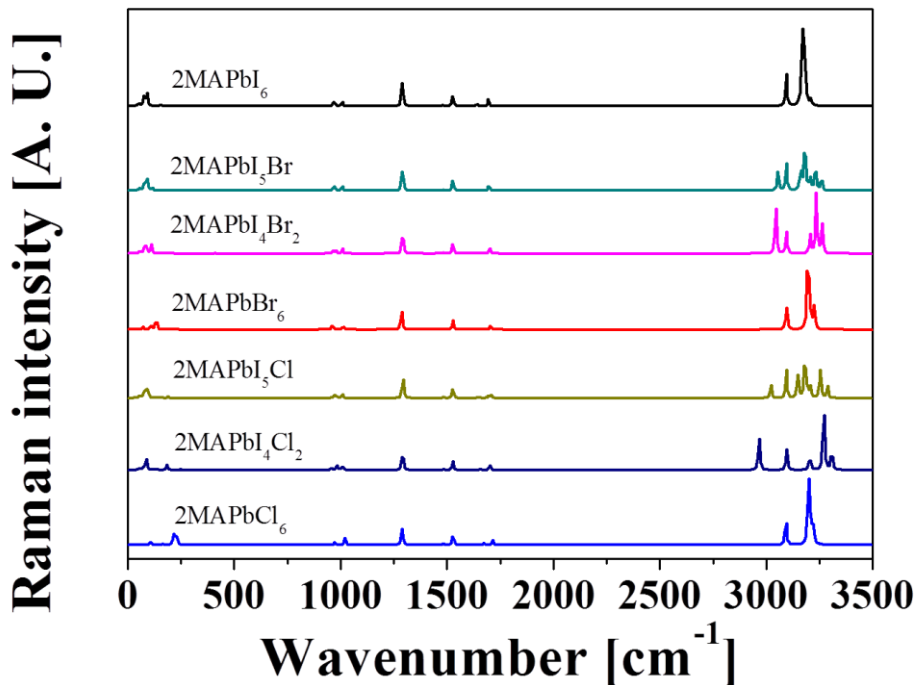


Figure S2. Theoretical Raman spectra for the model clusters.

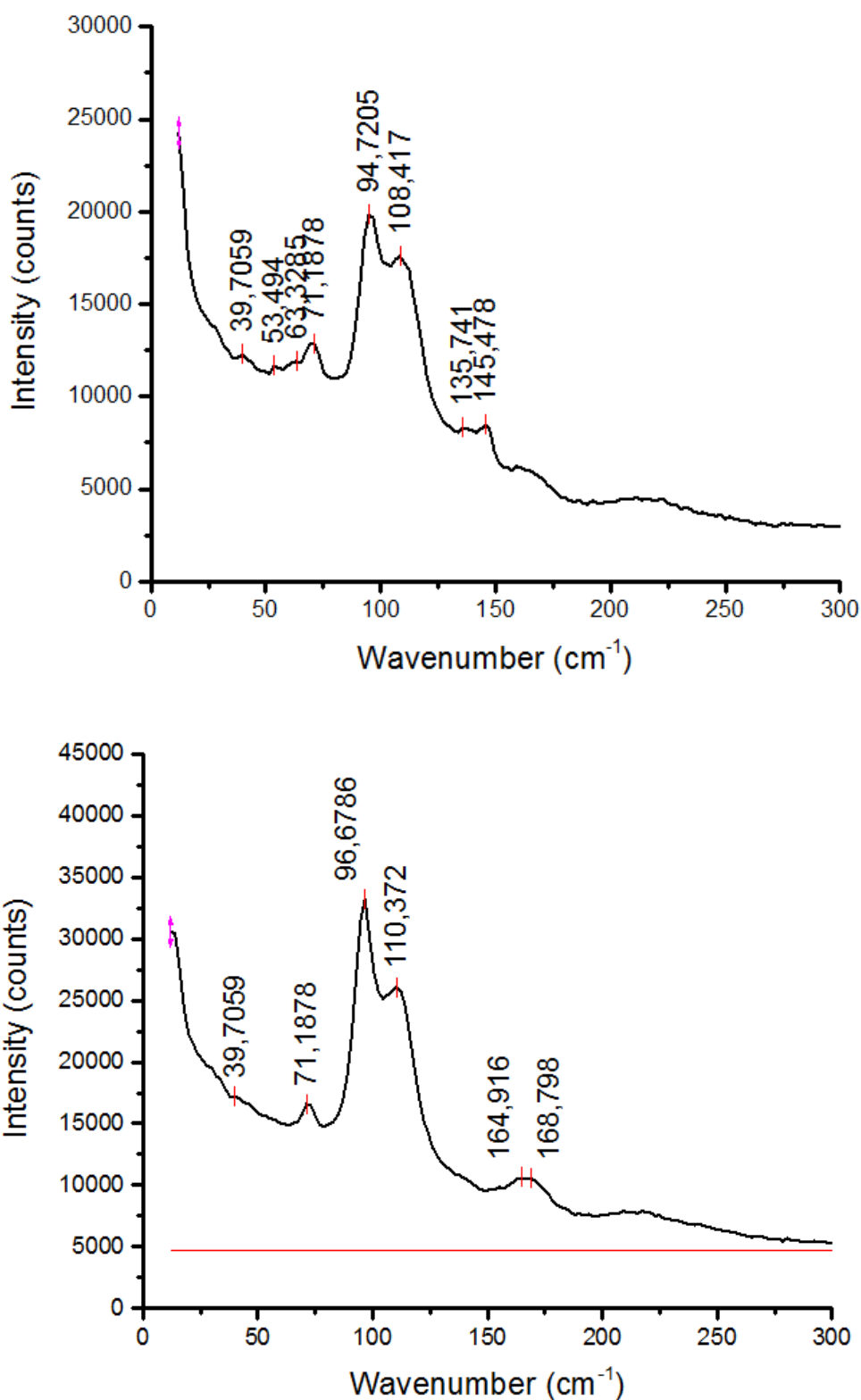


Figure S3. Experimental Raman spectra with peak identification of MAPbI₃ (top) and MAPbI₂Cl (bottom)

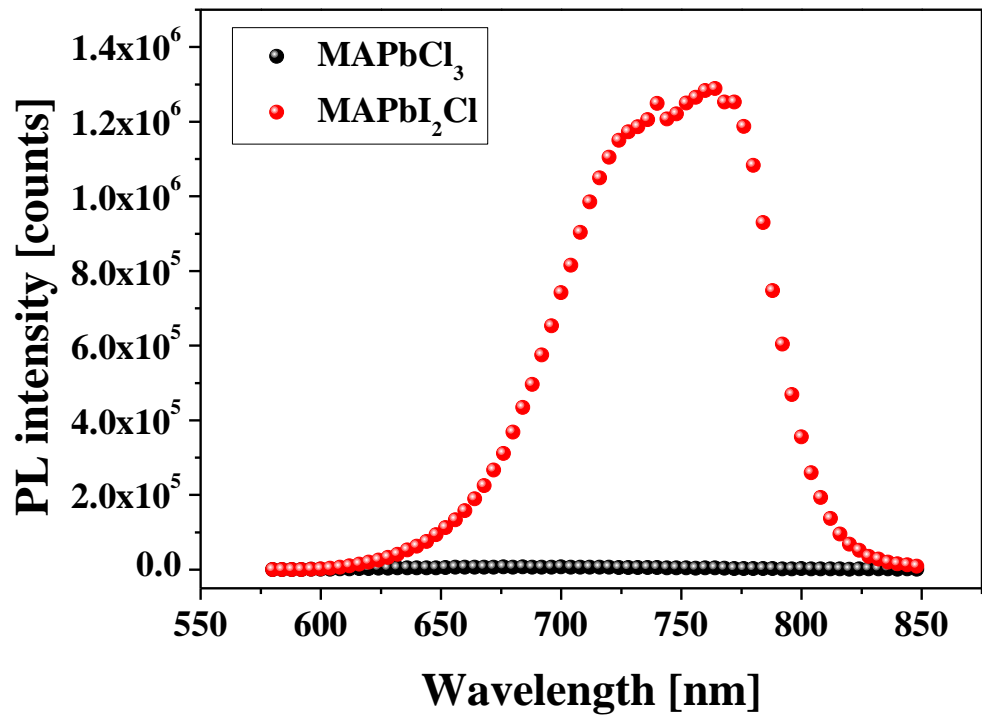


Figure S4. PL spectra of MAPbCl_3 and MAPbI_2Cl .

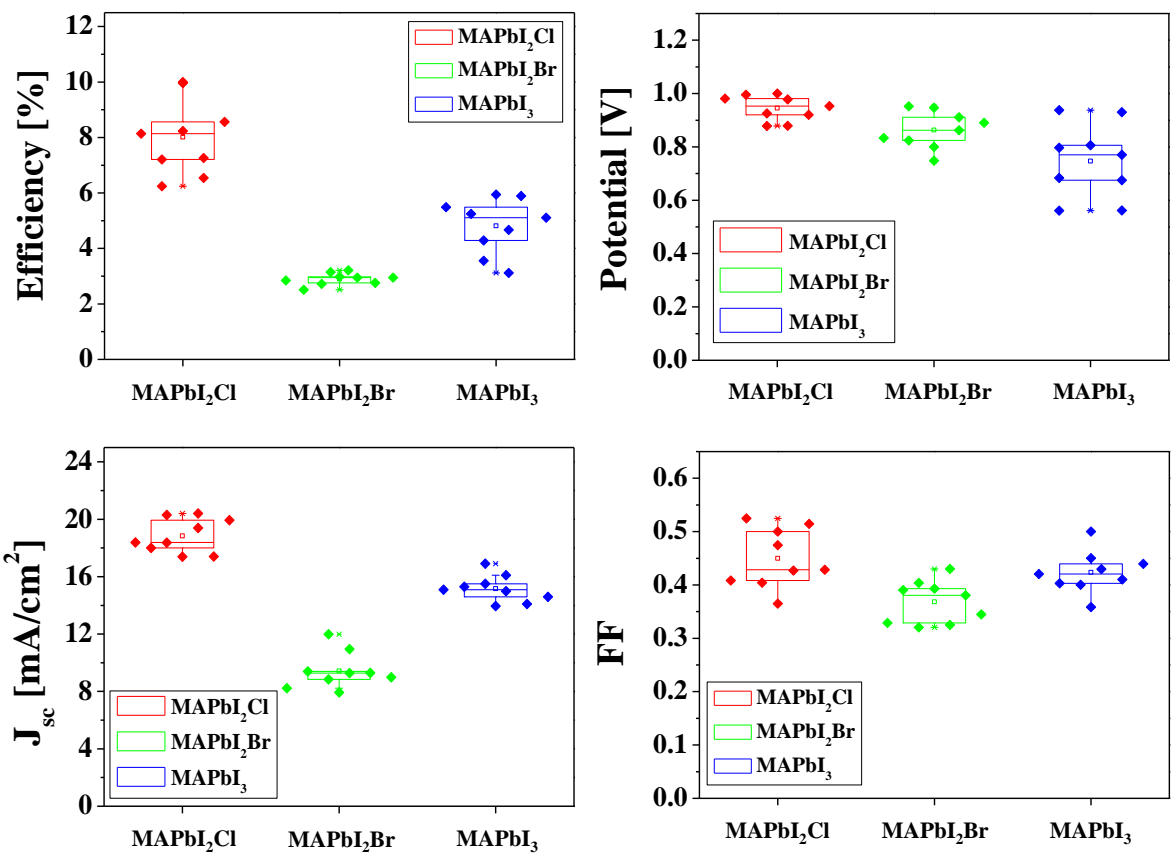


Figure S5. Distribution of solar cell performances on each one batch using mixed halide perovskite light absorbers for Figure 4(a)